Composite Structures 184 (2018) 1–10

Contents lists available at ScienceDirect

Composite Structures

journal homepage: www.elsevier.com/locate/compstruct

# Mechanical behavior of ultra-high toughness cementitious composite strengthened with Fiber Reinforced Polymer grid

Yu-Zhou Zheng[a,b,c], Wen-Wei Wang[a,*], Khalid M. Mosalam[b,c,*], Zhong-Feng Zhu[a]

[a] Department of Bridge Engineering, School of Transportation, Southeast University, Nanjing, China
[b] Department of Civil and Environmental Engineering, University of California, Berkeley, CA, USA
[c] Pacific Earthquake Engineering Research (PEER) Center, University of California, Berkeley, CA, USA

ARTICLE INFO

*Keywords:*
BFRP grid
Strengthening
Stress–strain relationship
Tensile force capacity
Tensile test
UHTCC

ABSTRACT

A new strengthening composite system, namely Basalt Fiber Reinforced Polymer (BFRP) grid – Ultra-High Toughness Cementitious Composite (UHTCC) for Reinforced Concrete (RC) structures is explored in this paper. Thirty UHTCC specimens internally strengthened with BFRP grid and six similar reference specimens without strengthening were tested to investigate the tensile mechanical behavior. The reinforcement ratio of the BFRP grid (0.17%, 0.68%, and 1.16%) and the mix proportion of the UHTCC were the two main test parameters. The experimental results highlighted two failure modes: 1) rupture or slip off failure of chopped PolyVinyl Alcohol (PVA) fibers at the critical crack sections in the reference specimens, and 2) partial rupture failure of BFRP grid within the UHTCC in all strengthened specimens. Moreover, the relative slip at the interface between the BFRP grid and the UHTCC substrate was not observed during testing. The tensile force capacity of the strengthened BFRP–UHTCC specimens increased by 42% to 172% compared to the reference specimens depending on the reinforcement ratio of the BFRP grid. On the other hand, the tensile force capacity of BFRP–UHTCC specimens slightly decreased by 1% to 14% with the increase of the water-to-cement material ratio of the UHTCC layer from 24% to 38%. Additionally, a stress–strain relationship and strength models of the strengthened specimens are proposed and verified with the test results to predict the tensile mechanical behavior.

## 1. Introduction

With the wide application of Fiber Reinforced Polymer (FRP) composite in strengthening Reinforced Concrete (RC) structures, a few of potential drawbacks have been presented by some researchers when using the Epoxy resin as the bonding and impregnated agent [1–5]. These drawbacks include debonding of interface, rapid aging, poor resistance to fire and ultraviolet (UV) light, etc [6]. In order to overcome such drawbacks, some researchers attempted to replace the organic matrix composite (e.g. Epoxy resin) with inorganic or cementitious materials to develop relatively new fiber composite reinforcing systems for strengthening RC structures. Examples of such attempts include Polymer Mortar [7,8], Mineral-based Composite [9,10], Fiber-Reinforced Inorganic Polymer (FRIP) [11,12], Textile Reinforced Mortars/Concrete (TRM/TRC) [13–19], and cement based dry fiber sheets [20–23]. These methods utilized many advantages of the used cementitious materials. Particularly, the engineered cement-based adhesive provided a much better material compatibility with the concrete substrate compared to the Epoxy-based ones.

Although the above-mentioned strengthening techniques improved the load carrying capacities and met functional requirements of structures under normal service condition, some deficiencies of the used strengthening materials remained. These deficiencies include incompatibility of deformation between the FRP reinforcement and the cement-based matrix, need for larger amounts of FRP reinforcement leading to increasing cost, poor penetration ability of the FRP sheet/plate, and low tensile strength and durability [24,25]. Therefore, a promising strengthening composite system, namely Basalt FRP (BFRP) grid – Ultra-High Toughness Cementitious Composite (UHTCC) for RC structures was explored [26–29]. This new strengthening composite system is expected to provide a dual enhancing effect to the original RC structures due to the high strength of the BFRP grid and the strain-hardening behavior of the UHTCC. Meanwhile, the UHTCC as a bonding agent is expected to suppress the width of cracks and prevent the crack-induced debonding failure due to the multiple cracking behavior of the UHTCC [30–32].

* Corresponding authors at: Department of Bridge Engineering, School of Transportation, Southeast University, China (W.W. Wang), Pacific Earthquake Engineering Research (PEER) Center, University of California, Berkeley, CA, USA (K.M. Mosalam).
*E-mail addresses:* universe2009@126.com, 230139502@seu.edu.cn (Y.-Z. Zheng), wangwenwei@seu.edu.cn (W.-W. Wang), mosalam@berkeley.edu (K.M. Mosalam), world789-001@163.com, 230149516@seu.edu.cn (Z.-F. Zhu).

http://dx.doi.org/10.1016/j.compstruct.2017.09.073
Received 25 July 2017; Received in revised form 19 September 2017; Accepted 26 September 2017
Available online 28 September 2017

Basic research should be conducted before the application of the BFRP grid–UHTCC strengthening system. This paper summarizes such basic research to develop the stress–strain relationship of the BFRP–UHTCC as a Composite Reinforcement Layer (CRL) to be used for future analytical simulation using finite element analysis to predict the flexural and shear load capacities of strengthened RC structures. In the presented study, an experimental program was conducted to investigate the mechanical behavior of the CRL under a uniaxial tensile load. Thirty UHTCC specimens internally strengthened with BFRP grid and a similar six reference specimens without strengthening were tested. The reinforcement ratio of the BFRP grid (0.17%, 0.68%, and 1.16%) and the mix proportion of the UHTCC were the two main test parameters. Moreover, a tensile stress–strain relationship and strength models of the CRL are proposed and validated with the test results to predict the mechanical behavior.

## 2. Experimental program

### 2.1. Specimen description

Thirty BFRP grid strengthening UHTCC (BFRP–UHTCC) specimens and six UHTCC specimens without strengthening were tested under a uniaxial tensile load to investigate the mechanical behavior. All test specimens had identical dimensions of 400 mm in length, 100 mm in width and 30 mm in depth, as shown in Fig. 1(a). Four thin square aluminium plates with dimensions of 100 mm × 100 mm × 2 mm were bonded with Epoxy resin to the two opposite sides of the UHTCC substrate at the end regions to make sure the test specimen could be tightly clamped by the tensile test machine, as shown in Fig. 1(a).

In the test program, the non-metallic BFRP grid with the geometric dimensions of 100 mm in width and 400 mm in length was internally embedded in the UHTCC layer. The BFRP grid used in this study was produced by Jiangsu Green Materials Vally New Material T & D Co., Ltd, China. The continuous basalt-based untwisted yarns were used as the reinforcement fibers, which were impregnated with Epoxy resins to form the elements arranged at 50 mm center to center along of the longitudinal and transverse directions of the BFRP grid, as shown in Fig. 1(b).

All test specimens were divided into six groups where each group had six identical specimens as listed in Table 1. Group U0 without strengthening was set as the reference group. The investigated variables in this program were the reinforcement ratio of the BFRP grid and the mix proportion of the UHTCC. Three different thickness of the BFRP grid were used to internally strengthen the UHTCC over-layer: 1 mm for group FU1, 3 mm for groups FU2, FU4, and FU5, and 5 mm for group FU3. In addition, three different mix proportion of the UHTCC were considered to investigate their effect on the tensile force capacity of the strengthened UHTCC specimens: M1 for groups FU1, FU2, and FU3, M2 for group FU2, and M3 for group FU5.

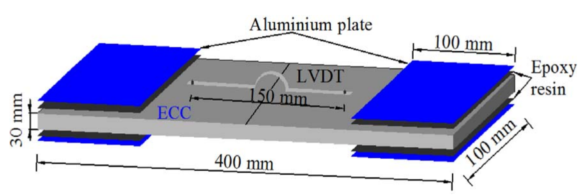


(a) BFRP–UHTCC specimen

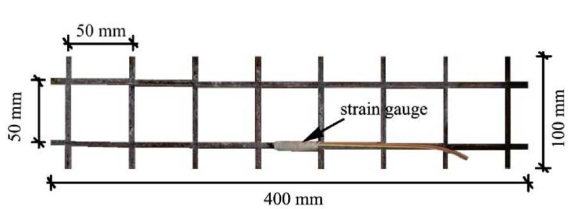


(b) BFRP grid

**Fig. 1.** Dimensions of the BFRP–UHTCC specimen and the BFRP grid. (a) BFRP-UHTCC specimen; (b) BFRP grid.

### 2.2. Test materials

The material tests of the UHTCC and BFRP grid were conducted to investigate the basic mechanical properties. For the UHTCC, Ordinary Portland cement (P.O 42.5 grade), fly ash (I grade), and silica fume with average diameter between 0.1 μm and 0.3 μm were used. Silica sand with gain size below 0.32 mm was selected as the fine aggregate and a modified polycarboxylic acid-based admixture was utilized as a water reducing agent. Chopped PolyVinyl Alcohol (PVA) fibers with length of 12 mm were used in the UHTCC mix. These fibers are produced by Kuraray Co., Ltd, Japan. The summary of the UHTCC mix designs are listed in Table 2.

The UHTCC material was placed into a steel mold to form the test specimen with dimensions of 400 mm in length, 200 mm in width and 30 mm in depth. During the casting process of the UHTCC, four cube samples with length dimension of 70.7 mm were cast to determine the UHTCC compressive strength for each mix proportion. After curing at a constant temperature of 20 ± 2 °C and relative humidity of 95% for 28 days, all cube samples were tested by a uniaxial compression test machine to determine the compressive strength. The 28-day average compressive strength of the UHTCC for each mix proportion are listed in Table 2.

Nine BFRP grid samples (three samples for each reinforcement ratio of BFRP grid) were tested to investigate the tensile behavior. All tested BFRP grid samples had the same geometrical dimensions as used in the BFRP–UHTCC specimens, as shown in Fig. 1(b). All BFRP grids exhibited a linear behavior until the partial rupture of the fiber reinforcement, as shown in Fig. 2. The average tensile strength of the 1 mm, 3 mm, and 5 mm thick BFRP grids were 357 MPa, 386 MPa, and 416 MPa, respectively. On the other hand, the average elastic modulus of these grids was 51 GPa, 53 GPa, and 57 GPa, respectively.

### 2.3. Test setup and instruments

After conditioned in a curing chamber with a constant temperature of 20 ± 2 °C and relative humidity of 95% for 28 days, all specimens were tested by a displacement-controlled uniaxial tensile test machine. One end of the tested specimen was firstly placed into the workspace of the steel collets in the universal testing machine, then another one was automatically clamped by the remaining two steel collets, as shown in Fig. 3. The rate of application of the uniaxial displacement was 0.5 mm/min during the whole test. One 'Ω' shape Linear Variable Displacement Transducer (LVDT) was bonded to one side surface of the test specimen to measure the axial deformation. The gauge length of the LVDT was 150 mm, as shown in Fig. 3. Moreover, one electrical resistance strain gauge with a length of 10 mm was attached to the surface of the BFRP grid at the middle section of the specimen to monitor the strain variation, as shown in Fig. 3. The external applied load, the axial deformation of the test specimen and the strain of the BFRP grid embedded in the UHTCC layer were all collected by an automatic data acquisition system.

## 3. Test results

### 3.1. Failure modes

Two failure modes of the strengthened specimens were observed in this test program. One mode was the typical fracture failure of UHTCC for the reference UHTCC specimens (i.e. Group U0) due to the internal chopped PVA fibers fractured or slip off from the cement substrate at

**Table 1**
Details of the test specimens.

| Group | 6 Specimens of | FRP grid | | | Mix of UHTCC | Dimensions [mm] |
|---|---|---|---|---|---|---|
| | | Fiber type | ratio [%] (thickness [mm]) | Tensile strength [MPa] | | |
| U0 | UHTCC | None | None | None | M1 | 400 × 100 × 30 |
| FU1 | BFRP–UHTCC | BFRP | 0.17 (1) | 357 | M1 | 400 × 100 × 30 |
| FU2 | BFRP–UHTCC | BFRP | 0.68 (3) | 386 | M1 | 400 × 100 × 30 |
| FU3 | BFRP–UHTCC | BFRP | 1.16 (5) | 416 | M1 | 400 × 100 × 30 |
| FU4 | BFRP–UHTCC | BFRP | 0.68 (3) | 386 | M2 | 400 × 100 × 30 |
| FU5 | BFRP–UHTCC | BFRP | 0.68 (3) | 386 | M3 | 400 × 100 × 30 |

**Table 2**
Mix proportions of the UHTCC.

| Mix | Water (W) [kg] | Cement (C) [kg] | Fly ash [kg] | Silica sand [kg] | PVA fiber volume content [%] | Silica fume [kg] | Water reducer [kg] | W/C [%] | Compressive strength [MPa] |
|---|---|---|---|---|---|---|---|---|---|
| M1 | 0.33 | 0.40 | 1.00 | 0.32 | 2 | 0.040 | 0.005 | 24 | 33 |
| M2 | 0.33 | 0.24 | 0.94 | 0.24 | 2 | 0.036 | 0.014 | 28 | 32 |
| M3 | 0.33 | 0.67 | 0.20 | 0.17 | 2 | 0.028 | 0.001 | 38 | 25 |

**Fig. 2.** Failure mode of the BFRP grid.

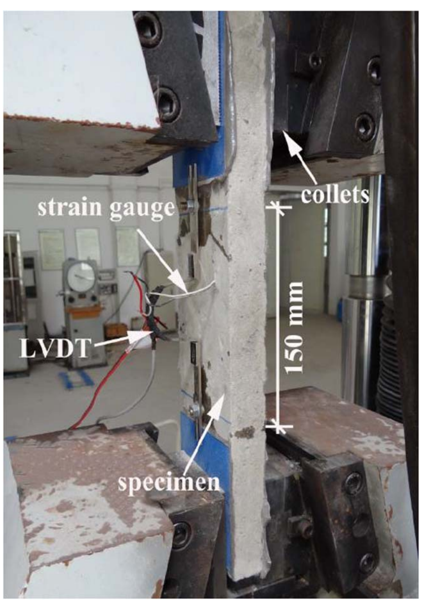


**Fig. 3.** Details of the test setup and instruments.

(a) UHTCC specimen

(b) BFRP–UHTCC specimen (1 mm FRP grid)

(c) BFRP–UHTCC specimen (3 mm FRP grid)

(d) BFRP–UHTCC specimen (5 mm FRP grid)

**Fig. 4.** Failure modes of test specimens. (a) UHTCC specimen; (b) BFRP–UHTCC specimen (1 mm FRP grid); (c) BFRP–UHTCC specimen (3 mm FRP grid); (d) BFRP–UHTCC specimen (5 mm FRP grid).

the critical crack section, as shown in Fig. 4(a). The other mode was the rupture failure of the BFRP grid for the strengthened BFRP–UHTCC specimens (i.e. Groups FU1 to FU5) due to one axial fiber reinforcement of the BFRP grid ruptured at the critical crack sections, as shown in Fig. 4(b) to (d). In addition, several fine cracks appeared on the surface of the UHTCC in the vicinity of middle section when the applied load approached the cracking strength of the UHTCC. These fine cracks propagated towards the two sides of the test specimen and widened with further increase of the applied load. When the BFRP–UHTCC specimens failed, there was no observed debonding at the interface between the BFRP grid and the UHTCC substrate, which indicated a good bonding and compatible behavior of the BFRP grid-to-UHTCC interface. Compared with the reference UHTCC specimens (i.e. Group U0), the numbers of fine cracks of the BFRP–UHTCC specimens (i.e. Groups FU1 to FU5) were obviously increased with the increase of the BFRP grid reinforcement ratio from 0.68% to 1.16% due to the reinforcement contribution of the BFRP grid, while the average spacing and width of the fine cracks were significantly decreased, as shown in Fig. 4.

For the reference specimens (i.e. Group U0) without the internal reinforcement of BFRP grid, when the applied tensile load reached

7.26 kN (the average cracking load of six specimens in same group) or approximately 86% of the ultimate load, a few of the fine cracks appeared at the middle section of the test specimen. In addition, with further increase of the external load, more fine cracks uniformly appeared along the axial direction of the specimen (cracks were perpendicular to the axis of the specimen) and propagated toward the two side edges of the specimen. As a result, the multiple point cracking phenomenon of UHTCC was clearly presented. When the tensile load reached 8.41 kN (the average ultimate load of six specimens in the group), the UHTCC specimen was separated into two parts at the critical cracked section. This was attributed to the internal chopped PVA fibers fracturing or pulling out from the cement substrate, as shown in Fig. 4(a), leading to complete failure of the UHTCC specimen.

For group FU1 strengthened with 1 mm thickness of BFRP grid, when the tensile load approached 8.17 kN (the average cracking load of six specimens in the group) or approximately 68% of the ultimate load, a few of fine cracks appeared on the surface of the UHTCC layer. Moreover, with further increase of the applied tensile load, new fine cracks formed and the existing fine cracks constantly propagated toward the two side edges of the BFRP–UHTCC specimen. When the applied load increased to 11.91 kN (the average ultimate load of six specimens in the group), “cracking” sound from the BFRP grid can be clearly heard and then one longitudinal fiber reinforcement of the BFRP grid was finally ruptured at the main cracked section, as shown in Fig. 4(b). For the other four strengthened BFRP–UHTCC specimen groups, i.e. FU2 to FU5, similar observations to those of specimen group FU1 took place with different numbers and spacing of fine cracks during testing.

### 3.2. Stress–strain relationships of test specimens

The tensile strain point of the test specimen just before cracking of the UHTCC is defined as the cracking strain and the corresponding tensile stress is defined as the cracking stress. Moreover, the key quantities corresponding to the cracking and ultimate states are summarized in Table 3. It should be noted that the tensile stress of the test specimen was obtained from $\sigma_{fu} = P_t/A_{fu}$ where $P_t$ is the applied tensile load and $A_{fu}$ is the cross-sectional area of the test specimen. In addition, the tensile strain of the test specimens, $\varepsilon_{fu} = \Delta L/L$, was deduced from the gauge increment of the LVDT, $\Delta L$, and its initial gauge length, $L$.

For illustrating the difference between the stress–strain relationships of the tested specimens, the tensile stress–strain responses of the BFRP grid and the UHTCC of the test specimen under the uniaxial load are presented in Fig. 5. It is clear that the tensile stress–strain relationships of all test specimens can be divided into two stages. In the first stage, the test specimens exhibit almost a linear behavior until the first crack appeared close to the middle section. The tangent slope of the stress–strain relationship is gradually reduced with further increase of the external load, which is mainly determined by the elastic modulus of the UHTCC during this stage. The second stage starts from the cracking of UHTCC layer to the failure of the test specimen. During this stage, the tensile strains of the test specimens are significantly improved with further increase of the external axial load. However, the increasing amplitude of the stress is much lower than the corresponding strain due to the multi-point cracking properties of the UHTCC.

For the reference group (U0) without strengthening, as shown in Fig. 5a, a larger strain was observed with the further increase of the external tensile load after the UHTCC cracked, while the corresponding tensile stress almost kept a constant level until the failure of the test specimen. Therefore, the well-known strain-hardening phenomena of UHTCC is clearly presented by this behavior. This is a significant advantage for the UHTCC compared to the normal concrete. For the strengthened BFRP–UHTCC specimens (i.e. Groups FU1 to FU5), as shown in Fig. 5b to 5f, the average axial stiffness of the test specimen was also at a high level after the UHTCC cracked due to the strengthening contribution of the internal BFRP grids. Additionally, larger ultimate tensile strains of the BFRP–UHTCC specimens were exhibited during the testing progress.

### 3.3. Analysis of test parameters

The effects of the BFRP grid reinforcement ratio and mix proportion of the UHTCC on the tensile behavior of the BFRP–UHTCC specimens are compared in terms of the cracking and ultimate loads of all test specimens as shown in Fig. 6. It should be noted that the load value of each group shown in Fig. 6 is the average load value of the six specimens in the same group. For groups FU1, FU2, and FU3 strengthened with different reinforcement ratios of BFRP grids (i.e. 0.17%, 0.68%, and 1.16%, respectively), the cracking and ultimate loads of groups FU1, FU2, and FU3 increased from 10% to 17%, and from 42% to 172%, respectively, compared to that of the reference Group U0, as shown in Fig. 6 and Table 3. It is clear that the BFRP–UHTCC specimens achieved a much higher tensile force capacity than the UHTCC specimens, as expected. This is attributed to the addition of the BFRP grid in the UHTCC layer. In addition, the tensile force capacities of the BFRP–UHTCC specimens greatly improved with further increase of the BFRP grid reinforcement ratio from 0.17% to 1.16%. However, the effect of the BFRP grid reinforcement ratio on the cracking load is much lower than that on the ultimate load, which indicated that the cracking load of the test specimen is mainly determined by the tensile strength of the UHTCC. The cause of this phenomenon is that the cracking strain of the UHTCC was small and the BFRP grid only played a small role in improving the cracking load of the test specimens. Additionally, the material properties of the BFRP grid and the UHTCC can be effectively utilized by using the BFRP grid strengthening the UHTCC as a composite reinforcement layer.

For groups FU2, FU4, and FU5 using different mix proportion of the UHTCC (i.e. M1, M2, and M3, respectively), the cracking and ultimate loads of groups FU4 and FU5 decreased from 6% to 26%, and from 4% to 18%, respectively, compared to that of group FU2, as shown in Fig. 6 and Table 3. Thus, it is observed that the tensile force capacity of the BFRP–UHTCC specimens slightly decreased with the mix proportion of the UHTCC changed from M1 to M3 due to the increase of the UHTCC water-to-cement material ratio from 0.24 to 0.38. Therefore, when using the spraying UHTCC (i.e. the mix proportion of M3) as the cement substrate for the BFRP–UHTCC structures, a higher reinforcement ratio of the BFRP grid should be considered in order to achieve an equivalent load capacity level of the BFRP-UHTCC with M1 mix proportion.

## 4. Analytical model

### 4.1. Predictive model

This section summarizes the development of the stress–strain model of the BFRP–UHTCC as a composite reinforcement layer (CRL) to be used for future simulations using the finite element method to predict the flexural and shear load capacities of strengthened RC structures. Therefore, a tensile stress–strain relationship and strength models of the BFRP–UHTCC specimen are proposed based on the previously discussed test results to predict the mechanical behavior.

Based on the experimental results of the BFRP–UHTCC specimens under the uniaxial tensile load, their tensile stress–strain relationship can be divided into two stages, as indicated in Fig. 7. This relationship is mathematically expressed as follows:

$$\sigma_{fu} = \begin{cases} A\varepsilon_{fu}^2 + B\varepsilon_{fu} + C & (0 \leqslant \varepsilon_{fu} \leqslant \varepsilon_{fu,cr}) \\ E_2(\varepsilon_{fu} - \varepsilon_{fu,cr}) + \sigma_{fu,cr} & (\varepsilon_{fu,cr} \leqslant \varepsilon_{fu} \leqslant \varepsilon_{fu,u}) \end{cases} \tag{1}$$

where $\varepsilon_{fu}$ is the tensile strain corresponding to the stress, $\sigma_{fu}$; $A$, $B$, and $C$ are the coefficients of the relationship for the first stage; $E_2$ is the tangent slope of the relationship for the second stage; $\varepsilon_{fu,cr}$ and $\varepsilon_{fu,u}$ are the cracking and ultimate strains, respectively; $\sigma_{fu,cr}$ is the cracking stress

**Table 3**
Comparisons of the test and calculated results.

| No. | Crack stage | | | | Ultimate stage | | | | | |
|---|---|---|---|---|---|---|---|---|---|---|
| | Test Strain $\varepsilon_{fu,cr}$ [$\mu\varepsilon$] | Test Load $P_{cr,t}$ [kN] | Calculated load $P_{cr,p}$ [kN] | $P_{cr,t}/P_{cr,p}$ | Test Strain $\varepsilon_{fu,u}$ [$\mu\varepsilon$] | Test Load $P_{u,t}$ [kN] | Calculated load $P_{u,p}$ [kN] | $P_{u,t}/P_{u,p}$ | FRP grid strain $\varepsilon_{f,u}$ [$\mu\varepsilon$] | $\varepsilon_{fu,u}/\varepsilon_{f,u}$ ($\beta$) |
| U0 | 368 | 7.50 | – | – | 11360 | 8.52 | – | – | – | – |
| | 443 | 8.28 | – | – | 10106 | 8.52 | – | – | – | – |
| | 308 | 7.95 | – | – | 9533 | 7.71 | – | – | – | – |
| | 432 | 8.40 | – | – | 9245 | 9.63 | – | – | – | – |
| | 293 | 4.71 | – | – | 8955 | 7.50 | – | – | – | – |
| | 363 | 6.57 | – | – | 13017 | 8.58 | – | – | – | – |
| FU1 | 480 | 8.70 | 10.22 | 0.85 | 10268 | 11.66 | 13.39 | 0.87 | 11343 | 0.91 |
| | 393 | 8.40 | 8.37 | 1.00 | 11188 | 11.10 | 11.87 | 0.94 | 11131 | 1.01 |
| | 434 | 9.00 | 9.24 | 0.97 | 10957 | 12.60 | 12.65 | 1.00 | 12856 | 0.85 |
| | 471 | 7.65 | 7.55 | 1.01 | 12622 | 12.27 | 11.49 | 1.07 | 14333 | 0.88 |
| | 452 | 7.86 | 7.24 | 1.09 | 11454 | 12.15 | 10.81 | 1.12 | 12221 | 0.94 |
| | 463 | 7.59 | 7.42 | 1.02 | 13275 | 12.12 | 11.58 | 1.05 | 16570 | 0.80 |
| FU2 | 390 | 9.03 | 8.63 | 1.05 | 11343 | 16.83 | 15.10 | 1.11 | 12128 | 0.94 |
| | 399 | 7.62 | 8.83 | 0.86 | 14192 | 18.06 | 16.98 | 1.06 | 12533 | 1.13 |
| | 364 | 7.08 | 8.05 | 0.88 | 16900 | 16.42 | 17.82 | 0.92 | 11153 | 1.52 |
| | 421 | 6.00 | 7.10 | 0.85 | 17819 | 16.20 | 17.38 | 0.93 | 11017 | 1.62 |
| | 499 | 8.16 | 8.42 | 0.97 | 15952 | 16.95 | 17.54 | 0.97 | 12763 | 1.25 |
| | 411 | 6.96 | 6.93 | 1.00 | 12843 | 16.27 | 14.27 | 1.14 | 10640 | 1.21 |
| FU3 | 364 | 7.53 | 8.39 | 0.90 | 20627 | 23.94 | 26.20 | 0.91 | 16042 | 1.29 |
| | 400 | 9.24 | 9.22 | 1.00 | 20038 | 21.87 | 26.48 | 0.83 | 15739 | 1.27 |
| | 373 | 9.39 | 8.60 | 1.09 | 16795 | 23.82 | 23.03 | 1.03 | 13621 | 1.23 |
| | 420 | 7.05 | 7.47 | 0.94 | 14910 | 21.21 | 20.21 | 1.05 | 11670 | 1.28 |
| | 506 | 9.36 | 9.00 | 1.04 | 17237 | 24.39 | 23.70 | 1.03 | 10571 | 1.63 |
| | 465 | 8.19 | 8.27 | 0.99 | 13882 | 23.40 | 20.06 | 1.17 | 9614 | 1.44 |
| FU4 | 395 | 7.83 | 10.46 | 0.75 | 12625 | 14.28 | 17.69 | 0.81 | 11630 | 1.09 |
| | 297 | 7.41 | 7.87 | 0.94 | 15570 | 17.76 | 16.89 | 1.05 | 12184 | 1.28 |
| | 359 | 7.14 | 9.51 | 0.75 | 14415 | 15.66 | 17.81 | 0.88 | 12019 | 1.20 |
| | 525 | 8.73 | 8.54 | 1.02 | 15953 | 18.48 | 17.65 | 1.05 | 11630 | 1.09 |
| | 472 | 7.08 | 7.68 | 0.92 | 13175 | 15.00 | 15.18 | 0.99 | 12184 | 1.28 |
| | 500 | 6.75 | 8.13 | 0.83 | 15980 | 15.12 | 17.28 | 0.88 | 12019 | 1.20 |
| FU5 | 662 | 6.90 | 7.45 | 0.93 | 16489 | 14.16 | 16.80 | 0.84 | 16826 | 0.98 |
| | 577 | 6.30 | 6.49 | 0.97 | 16467 | 13.38 | 15.88 | 0.84 | 11805 | 1.39 |
| | 551 | 6.90 | 6.20 | 1.11 | 14809 | 12.69 | 14.62 | 0.87 | 12779 | 1.16 |
| | 427 | 4.71 | 4.77 | 0.99 | 14752 | 14.19 | 13.24 | 1.07 | 12318 | 1.20 |
| | 534 | 5.43 | 5.97 | 0.91 | 15826 | 15.63 | 15.00 | 1.04 | 10907 | 1.45 |
| | 483 | 4.98 | 5.40 | 0.92 | 13755 | 12.69 | 13.24 | 0.96 | 8760 | 1.57 |
| Average | | | | 0.97 | | | | 0.98 | | 1.19 |
| Standard Deviation (SD) | | | | 0.10 | | | | 0.10 | | |
| Coefficient of Variation (COV) | | | | 0.11 | | | | 0.10 | | |

corresponding to $\varepsilon_{fu,cr}$.

The coefficients of $A$, $B$, and C, and the tangent slope $E_2$ should be firstly determined. As shown in Fig. 8, an uncracked BFRP–UHTCC specimen can be treated as a composite of the UHTCC substrate and the internal reinforcement of the BFRP grid. Applying the equilibrium conditions of the axial forces acting on a unit segment with the cross-section of the BFRP–UHTCC specimen, the following equation is deduced,

$$E_{fu}\varepsilon_{fu}A_{fu} = E_u\varepsilon_u A_u + E_f\varepsilon_f A_f \tag{2}$$

where $E_{fu}$, $E_u$, and $E_f$ are the elastic moduli of the BFRP–UHTCC specimen, the UHTCC layer and the BFRP grid, respectively; $\varepsilon_{fu}$, $\varepsilon_u$ and $\varepsilon_f$ are the tensile strain of the BFRP–UHTCC specimen, the UHTCC layer and the BFRP grid, respectively; $A_{fu}$, $A_u$, and $A_f$ are the cross-sectional area of the BFRP–UHTCC specimen, the UHTCC layer and the BFRP grid, respectively.

According to the stress analysis of the test results of the BFRP–UHTCC specimens summarized in Fig. 5, the strain of the BFRP grid was almost equal to that of the test BFRP–UHTCC specimen before the UHTCC cracked, i.e. $\varepsilon_{fu} = \varepsilon_u = \varepsilon_f$. Thus, Eq. (2) can be rewritten as follows,

$$E_{fu} = E_u + E_f\frac{A_f}{A_{fu}} \tag{3}$$

It is well known that the elastic modulus of the BFRP–UHTCC specimen could be affected by the stress softening characteristic of the UHTCC, the bonding performance of the interface between the chopped PVA fibers and the UHTCC cementitious base, and other inevitable test factors. It should be noted from Fig. 7 that the boundary conditions of the stress–strain relationship model of the BFRP–UHTCC specimens based on the test results are as follows, the tensile stress of the BFRP–UHTCC specimens at the point (0, 0) should be zero, and the tangent modulus of the stress–strain relationship at the point (0, 0) should be equal to the elastic modulus of the BFRP–UHTCC specimen, $E_{fu}$, i.e., the first derivative of the stress–strain relationship at the point (0, 0) is $E_{fu}$. Moreover, the proposed stress–strain relationship model in this section is a continues function. Thus, the tangent modulus of the stress–strain relationship at the point ($\varepsilon_{fu,cr}$,$\sigma_{fu,cr}$) should be equal to the equivalent stiffness of the BFRP–UHTCC specimen for the second stage. For simplify, the stiffness of the UHTCC was not considered in the second stage due to the quite small contribution to the stiffness of the FRP-UHTCC. Accordingly, the following equations can be deduced:

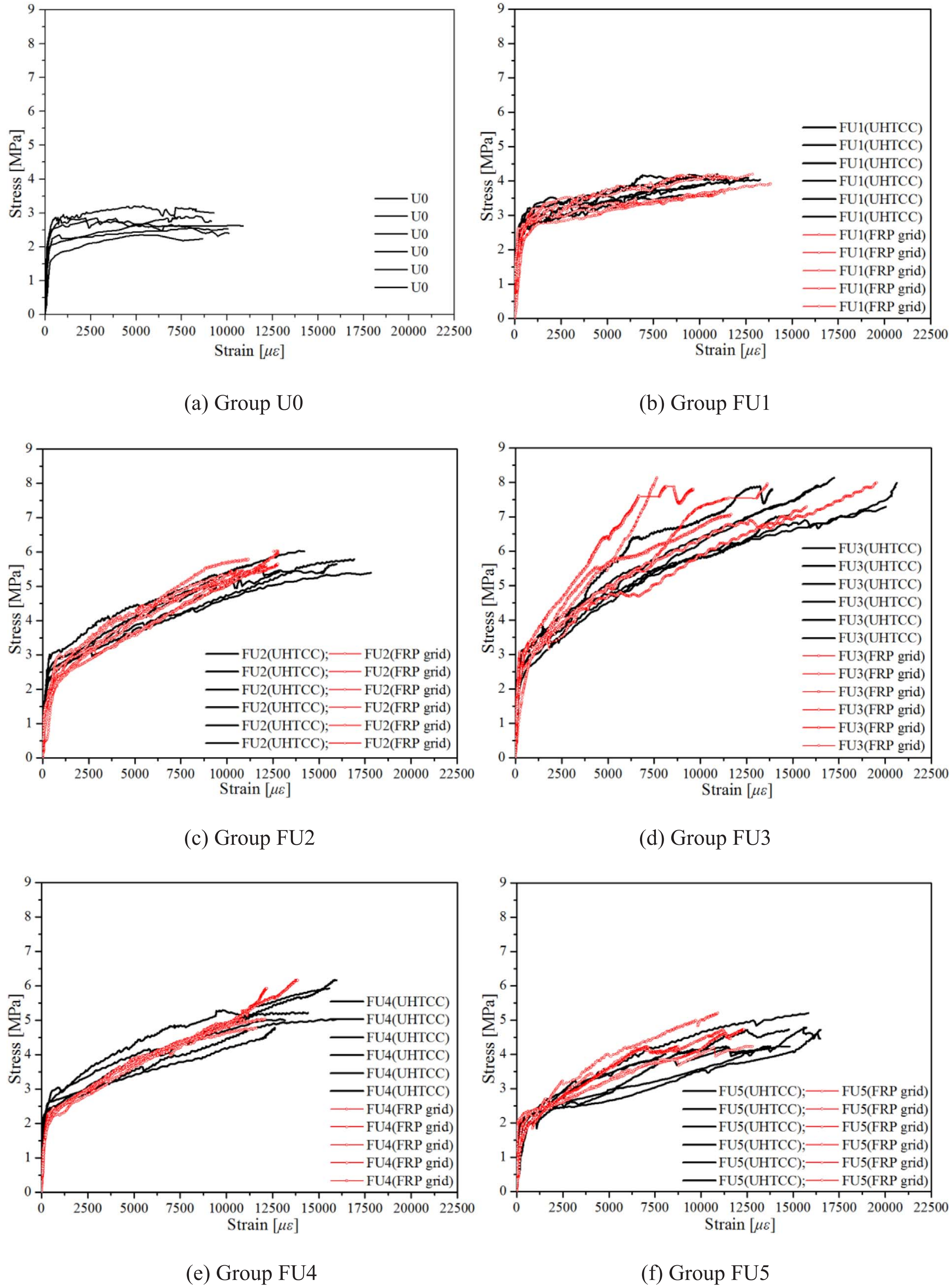


**Fig. 5.** Stress–strain relationships of the test specimens (six identical specimens in each group). (a) Group U0; (b) Group FU1; (c) Group FU2; (d) Group FU3; (e) Group FU4; (f) Group FU5.

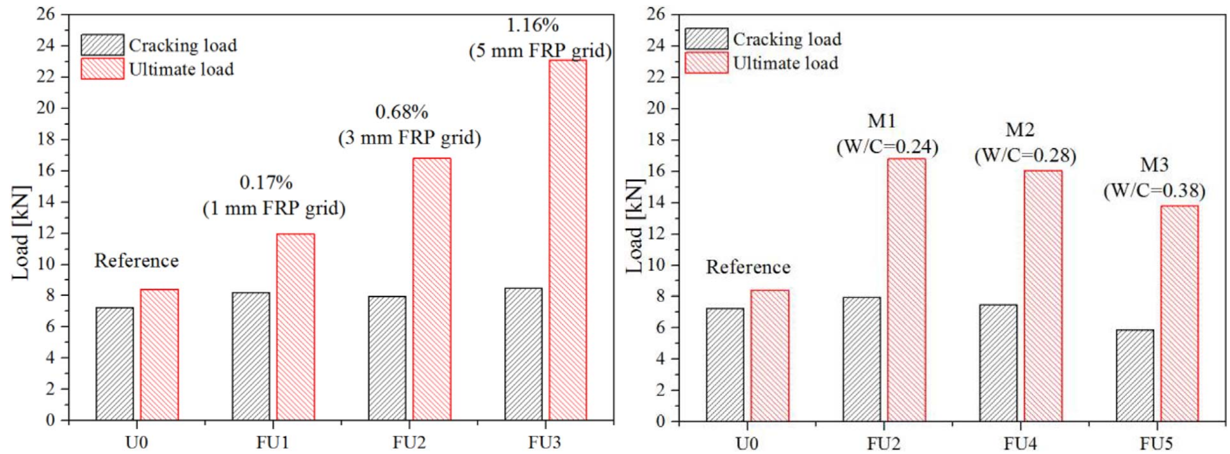


(a) Different reinforcement ratio of the BFRP grid (b) Different mix proportion of the UHTCC

**Fig. 6.** Comparison of the crack and ultimate loads of the test specimens. (a) Different reinforcement ratio of the BFRP grid; (b) Different mix proportion of the UHTCC.

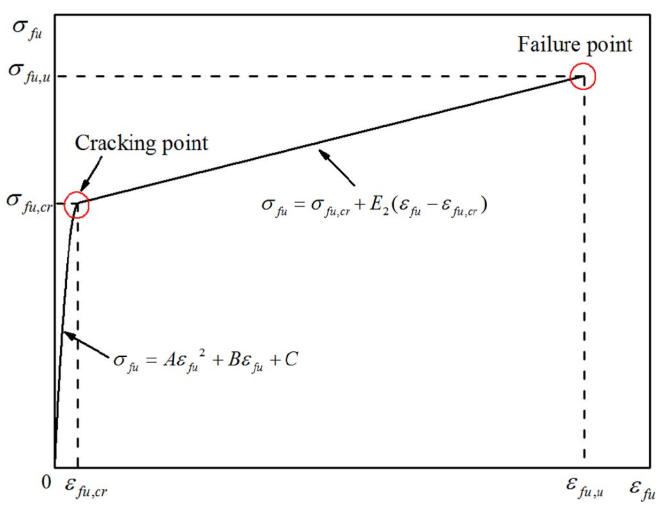


**Fig. 7.** Proposed stress–strain relationship model of the BFRP-UHTCC.

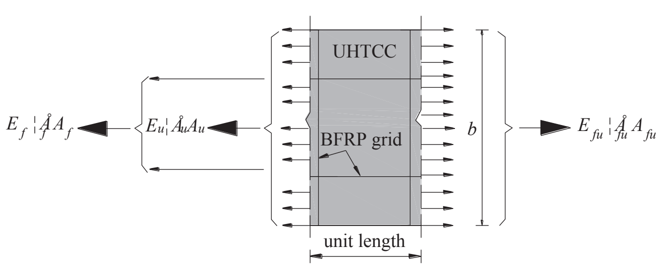


**Fig. 8.** Stress analysis of a segment with unit length and shown cross-section. (Equivalent equilibrium theory of the axial forces).

$$\begin{cases} \sigma_{fu}(0,0) = 0 \\ \left.\dfrac{d\sigma_{fu}}{d\varepsilon_{fu}}\right|_{(0,0)} = E_{fu} \\ \left.\dfrac{d\sigma_{fu}}{d\varepsilon_{fu}}\right|_{(\varepsilon_{fu,cr},\sigma_{fu,cr})} = E_f A_f/A_{fu} \end{cases} \quad (4)$$

Substituting Eqs. (1), (2), and (3) into Eq. (4), the coefficients $A$, $B$, and $C$ are obtained as follows,

$$\begin{cases} A = -\frac{E_u}{2\varepsilon_{fu,cr}} \\ B = E_u + E_f A_f/A_{fu} \\ C = 0 \end{cases} \quad (5)$$

As shown in Fig. 5, the tensile stress of the non-strengthened UHTCC specimens increased much smaller than that of the BFRP–UHTCC specimen after the UHTCC cracked. Moreover, in the BFRP–UHTCC strengthening system, only the UHTCC has significant strain-hardening, and the BFRP grid exhibits a linear behavior until the partial rupture of the fiber reinforcements. Therefore, the tangent slope of the stress–-strain relationship, $E_2$, at the second stage is mainly determined by the average axial stiffness of the BFRP–UHTCC specimen, which is dominated by the elastic modulus of the BFRP grid. Thus, the tangent slope, $E_2$, can be obtained through regressing the measured values of the $E_2$ and the average axial stiffness of the BFRP–UHTCC specimen, $E_f A_f/A_{fu}$, beyond the cracking strength of UHTCC, as shown in Fig. 9. This regression relationship is as follows,

$$E_2 = 0.32 E_f A_f/A_{fu} + 80.65 \quad (6)$$

Accordingly, Eq. (1) can be rewritten as follows:

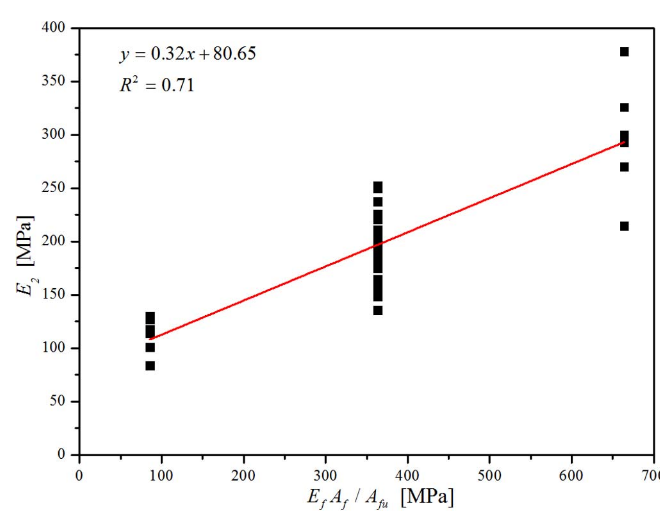


**Fig. 9.** Regression of the tangent slope $E_2$. (a liner fit may not be the best but chosen for simplicity).

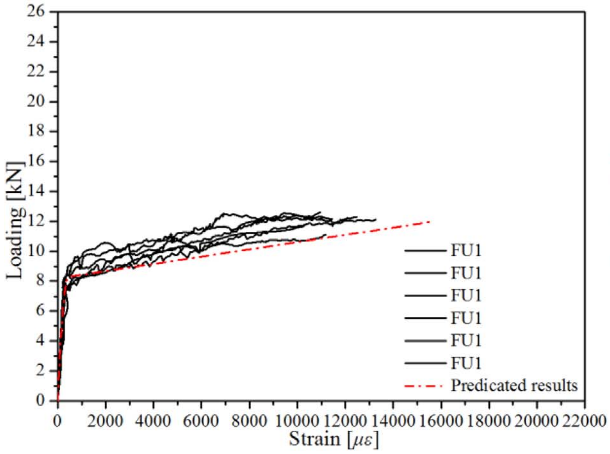


(a) Group FU1

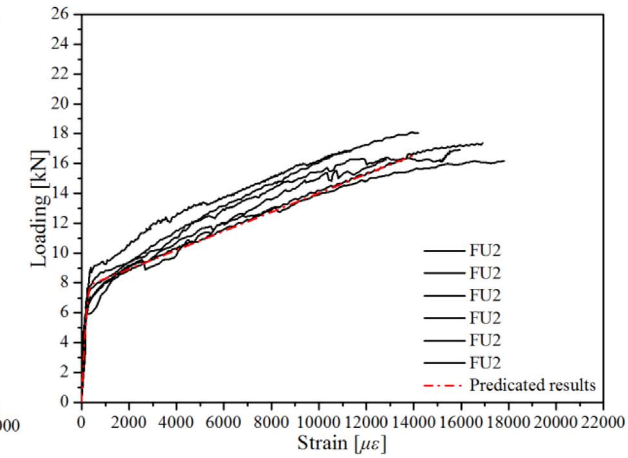


(b) Group FU2

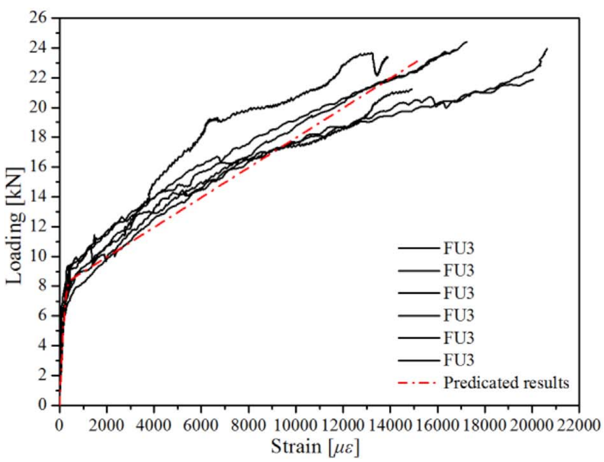


(c) Group FU3

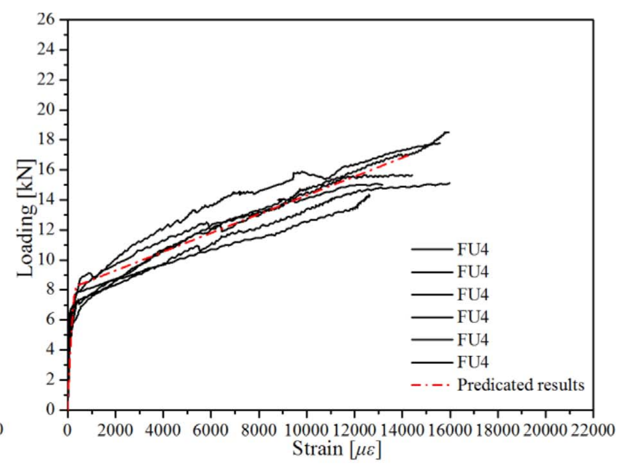


(d) Group FU4

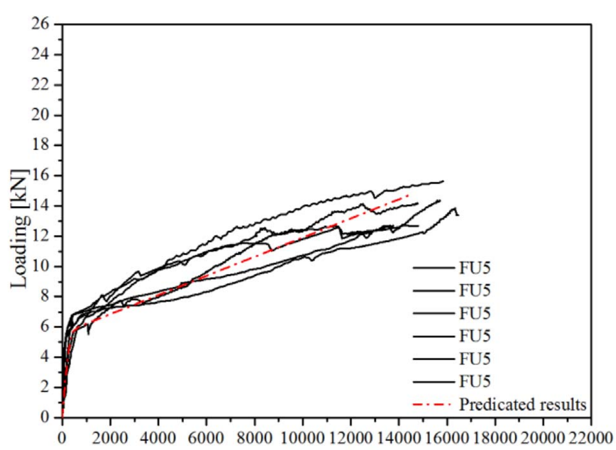


(e) Group FU5

**Fig. 10.** The comparisons of experimental results and the predictive model. (a) Group FU1; (b) Group FU2; (c) Group FU3; (d) Group FU4; (e) Group FU5.

$$\sigma_{fu}=\begin{cases}-\frac{E_u}{2\varepsilon_{fu,cr}}\varepsilon_{fu}^2+\left(E_u+\frac{E_fA_f}{A_{fu}}\right)\varepsilon_{fu} & (0\leqslant\varepsilon_{fu}\leqslant\varepsilon_{fu,cr})\\ \sigma_{fu,cr}+\left(0.32E_f\frac{A_f}{A_{fu}}+80.65\right)(\varepsilon_{fu}-\varepsilon_{fu,cr}) & (\varepsilon_{fu,cr}\leqslant\varepsilon_{fu}\leqslant\varepsilon_{fu,u})\end{cases} \quad (7)$$

As discussed above, the cracking stress of the BFRP–UHTCC specimen was primarily determined by the tensile strength of the UHTCC cementitious base. Therefore, the cracking strain of the BFRP–UHTCC specimen is assumed to be equal to that of the non-strengthened UHTCC specimens, such that, $\varepsilon_{fu,cr}=\varepsilon_{u,cr}$, where $\varepsilon_{u,cr}$ is the crack strain of the UHTCC layer. Whereas, the ultimate strain of the BFRP–UHTCC specimen was mainly dependent on the ultimate strength of the BFRP grid. After completing the statistical analysis of the measured ultimate strain of the BFRP–UHTCC specimen, the relationship between the ultimate strain of the BFRP–UHTCC specimen and the BFRP grid is established as follows:

$$\varepsilon_{fu,u}=\beta\varepsilon_{f,u} \quad (8)$$

where, $\varepsilon_{fu,u}$ and $\varepsilon_{f,u}$ are the ultimate strain of the BFRP–UHTCC specimen and the BFRP grid, respectively. $\beta$ is an empirical coefficient of the ultimate strain, $\beta=\varepsilon_{fu,u}/\varepsilon_{f,u}$, and the average value of this empirical coefficient, $\beta$, is determined to be 1.19, as shown in Table 3.

After the stress–strain relationship model of the BFRP–UHTCC specimen was determined, the predictive cracking load, $P_{cr,p}$, and ultimate load, $P_{u,p}$, can be respectively given as:

$$\begin{cases}P_{cr,p}=0.5E_u\varepsilon_{fu,cr}A_{fu}+E_f\varepsilon_{fu,cr}A_f\\ P_{u,p}=(0.5E_uA_{fu}+0.68E_fA_f-80.65A_{fu})\varepsilon_{fu,cr}+(0.32E_fA_f+80.65A_{fu})\varepsilon_{fu,u}\end{cases} \quad (9)$$

### 4.2. Model verification

The comparisons of the characteristic values, including the cracking and ultimate loads of all BFRP–UHTCC specimens under uniaxial tensile load are listed in Table 3. In addition, comparisons between the measured load–strain relationships of the BFRP–UHTCC specimens and the calculated ones using the predictive model are also presented in Fig. 10. As shown in Table 3 and Fig. 10, the predicted cracking and ultimate loads of the BFRP–UHTCC specimens follow the experimental ones very well with some minor discrepancies. Additionally, the average ratios of the experimental values to the predicted ones are 0.97 and 0.98 for the cracking and ultimate load, respectively, and the coefficient of variation (COV) is 0.11 for the crack loading, and 0.10 for the ultimate load, respectively. Therefore, the accuracy of the proposed model for predicting the stress–strain relationship and the tensile strength model of the BFRP–UHTCC specimen under uniaxial tensile loading are validated. It should be noted that only thirty-six experimental data sets were used for the validation in this case, which may raise the concern with the results of validation are rather trivial. Thus, we will collect and try other data sets to validate this stress–strain relationship of BFRP–UHTCC in the future.

## 5. Conclusions

A new strengthening technique using the BFRP grid and the UHTCC as a composite reinforcement layer for the RC structures is proposed in this paper. Thirty such BFRP–UHTCC specimens and six similar reference UHTCC samples without strengthening were tested to investigate the tensile mechanical performance of the BFRP–UHTCC under the uniaxial load. Based on the experimental observations, the following conclusions can be drawn:

1) The final failure modes of the five strengthened BFRP–UHTCC groups were the partial rupture of the fiber reinforcement at the critical crack sections due to the low tensile strength of the BFRP grid. As expected, the fracture failure of the UHTCC was occurred in the reference group due to the internal chopped PVA fibers ruptured or slip off from the cement substrate.
2) The tensile force capacities of the BFRP–UHTCC specimens were greatly improved after internally strengthened with the BFRP grid compared to the reference UHTCC samples. In addition, the tensile force capacity of those strengthened BFRP–UHTCC specimens increased by 42% to 172% compared to the reference UHTCC samples depending on the reinforcement ratio of the BFRP grid, which varied from 0.17% to 1.16%.
3) The tensile force capacity of BFRP–UHTCC specimens were slightly decreased by 4–18% with the increase of the UHTCC water-to-cement material ratio from 24% to 38%. Therefore, when using the spraying UHTCC (i.e. the mix proportion of M3) as the cement substrate for BFRP–UHTCC structures, a higher reinforcement ratio of the BFRP grid should be considered in order to achieve an equivalent load level.
4) An analytical model is also proposed to predict the stress–strain response and strength of the BFRP–UHTCC specimen, which was validated through comparison with the test results.

## Acknowledgements

The authors would like to express their gratitude to the National Natural Science Foundation of China – China (Program No.51278441 and 51578135), Graduate Scientific Research and Innovation Project of Jiangsu province, China – China (Program No. KYLX15_0142), China Scholarship Council – China (Program No. 201606090126) and University of California, Berkeley – USA for providing funding for this research work.

## References

[1] Zhang L, Wang WW, Harries KA, et al. Bonding behavior of wet-bonded GFRP-Concrete Interface. J Compos Constr 2014;19(6):04015001.
[2] Wang WW, Dai JG, Harries KA. Performance evaluation of RC beams strengthened with an externally bonded FRP system under simulated vehicle loads. J Bridge Eng 2013;18(1):76–82.
[3] Wang WW, Dai JG, Harries KA. Intermediate crack-induced debonding in RC beams externally strengthened with prestressed FRP laminates. J Reinf Plast Compos 2013;32(23):1842–57.
[4] Wang WW, Li G. Experimental study and analysis of RC beams strengthened with CFRP laminates under sustaining load. Int J Solids Struct 2006;43(6):1372–87.
[5] Wang WW, Dai JG, Harries KA, Bao QH. Prestress losses and flexural behavior of reinforced concrete beams strengthened with posttensioned CFRP sheets. J Compos Constr 2012;16:207–16.
[6] Gao WY, Teng JG, Dai JG. Effect of temperature variation on the full-range behavior of FRP-to-Concrete bonded joints. J Compos Constr 2012;16:671–83.
[7] Shi LY, Ai J, Gong CY, Chen ZH. Experimental research on shear behaviors of reinforced concrete beam strengthened with advanced glass fiber composites. Earthquake Eng Eng Vibr 2003;23(4):73–7. (In Chinese).
[8] Giustozzi F. Polymer-modified pervious concrete for durable and sustainable transportation infrastructures. Constr Build Mater 2016;111:502–12.
[9] Taljsten B, Blanksvard T. Mineral-based bonding of carbon FRP to strengthen concrete structures. J Compos Constr 2007;11(2):120–8.
[10] Blanksvard T, Taljsten B, Carolin A. Shear strengthening of concrete structures with the use of mineral-based composites. J Compos Constr 2009;13(1):25–34.
[11] Dai JG, Munir S, Ding Z. Comparative study of different cement-based inorganic pastes towards the development of FRIP strengthening technology. J Compos Constr 2014;18(3):A4013011.
[12] Ding Z, Dai JG, Muner S. Study on an improved phosphate cement binder for the development of fiber-reinforced inorganic polymer composites. Polymers 2014;6(11):2819–31.
[13] Zhang J, Wang ZB, Ju XC, Shi ZJ. Simulation of flexural performance of layered ECC-concrete composite beam with fracture mechanics model. Eng Fract Mech 2014;131:419–38.
[14] Verbruggen S, Aggelis DG, Tysmans T, Wastiels J. Bending of beams externally reinforced with TRC and CFRP monitored by DIC and AE. Compos Struct 2014;112:113–21.
[15] Larrinaga P, Chastre C, Biscaia HC, San-José JT. Experimental and numerical modeling of basalt textile reinforced mortar behavior under uniaxial tensile stress. Mater Des 2014;55:66–74.
[16] Tsesarsky M, Peled A, Katz A, Anteby I. Strengthening concrete elements by confinement within textile reinforced concrete (TRC) shells-Static and impact properties. Constr Build Mater 2013;44:514–23.
[17] Mechtcherine V. Novel cement-based composites for the strengthening and repair of concrete structures. Constr Build Mater 2013;41:365–73.

[18] Mechtcherine V. Towards a durability framework for structural elements and structures made of or strengthened with high-performance fiber-reinforced composites. Constr Build Mater 2012;31:94–104.

[19] Bu LT, Chen J, Lu C. Experiment on full-scale RC beam reinforced by polyvinyl alcohol-engineered cementitious composite mortar in flexure subjected to secondary load. J Hunan Univ (Nat Sci) 2011;1(38):1–8.

[20] Hashemi S, Al-Mahaidi R. Cement based bonding material for FRP strengthening of concrete structures. In: Proceedings of the 9th International Symposium on Fiber-reinforced Polymer Reinforcement for Concrete Structures (FRPRCS-9), Sydney, Australia 2009.

[21] Toutanji H, Zhao L, Zhang Y. Flexural behavior of reinforced concrete beams externally strengthened with CFRP sheets bonded with an inorganic matrix. Eng Struct 2006;28(4):557–66.

[22] Kurtz S, Palaguru P. Comparison of inorganic and organic matrices for strengthening of RC beams with carbon sheets. J Struct Eng 2001;127(1):35–72.

[23] Kolsch H. Carbon fiber cement matrix (CFCM) overlay system for masonry strengthening. J Compos Constr 1998;12(2):105–9.

[24] Dehghani A, Nateghi-Alahi F, Fischer G. Engineered cementitious composites for strengthening masonry infilled reinforced concrete frames. Eng Struct 2015;105:197–208.

[25] Kim YY, Lee BY, Bang J, et al. Flexural performance of reinforced concrete beams strengthened with strain-hardening cementitious composite and high strength reinforcing steel bar. Compos B Eng 2014;56:512–9.

[26] Zheng YZ, Wang WW. Tensile behavior of FRP grid strengthening ECC composite under a uniaxial loading. In: Second International Conference on Performance-based and Lifecycle Structural Engineering (PLSE 2015), Brisbane, Austria 2015.

[27] Zheng YZ, Wang WW, Brigham JC. Flexural behaviour of reinforced concrete beams strengthened with a composite reinforcement layer: BFRP grid and ECC. Constr Build Mater 2016;115:424–37.

[28] Zheng YZ, Wang WW, Li JF, Han GY. The constitutive relationship model of ECC composite strengthened with FRP grid under axial loading. Ind Constr 2016;46(5):12–7. (In Chinese).

[29] Wang WW, Zheng YZ. Experimental research on shear capacity of concrete beams strengthened with BFRP Grid reinforced ECC. In: Proceedings of the 9th National Construction Engineering Application of FRP Academic Communication, Chongqiong, China 2015. (In Chinese).

[30] Huang X, Ranade R, Zhang Q, et al. Mechanical and thermal properties of green lightweight engineered cementitious composites. Constr Build Mater 2013;48:954–60.

[31] Soe KT, Zhang YX, Zhang LC. Impact resistance of hybrid-fiber engineered cementitious composite panels. Compos Struct 2013;104:320–30.

[32] Cho C, Kim Y, Feo L, Hui D. Cyclic responses of reinforced concrete composite columns strengthened in the plastic hinge region by HPFRC mortar. Compos Struct 2012;94:2246–53.